Electrochemical-Mechanical Coupling Failure Mechanism of Composite Cathode in All-Solid-State Batteries

Chunhao Yuan[1,2], Wenquan Lu[3], Jun Xu[1,2,4*]

[1]*Department of Mechanical Engineering and Engineering Science, The University of North Carolina at Charlotte, Charlotte, NC 28223, USA*

[2]*Vehicle Energy & Safety Laboratory (VESL), The University of North Carolina at Charlotte, Charlotte, NC 28223, USA*

[3]*Chemical Sciences and Engineering Division, Argonne National Laboratory, Lemont, IL 60439, USA*

[4]*School of Data Science, The University of North Carolina at Charlotte, Charlotte, NC 28223, USA*

[*]Correspondence to: jun.xu@uncc.edu. Lead author: Prof. Jun Xu, Email: jun.xu@uncc.edu

Abstract: Composite cathode composed of active particles and solid electrolytes (SEs) can considerably enlarge the particle-SE contact areas and achieve high areal loadings in all-solid-state batteries (ASSBs). However, the challenging interfacial instability and particle damage problems remain unsolved. Herein, we establish a 3D electrochemical-mechanical coupled model to investigate the underlying failure mechanism by considering the governing electrochemical and physics processes. Micro-scale heterogeneous primary particles with random crystallographic orientation and size inside the $LiNi_{1/3}Co_{1/3}Mn_{1/3}O_2$ (NCM111) secondary particle of the model result in the anisotropic Li diffusion and volume variation within the secondary particle, leading to significant nonuniformity of the Li concentration, and GPa-level stress distributions at primary particle boundaries, and finally causing the particle internal cracks. The particle volume shrinkage under the constraint of stiff $Li_7La_3Zr_2O_{12}$ (LLZO) SE triggers the interface debonding (gap>50 nm) with increased interfacial impedance to degrade cell capacity. Higher C-rates result in larger residual stress (~100MPa)/strain/debonding gap at discharging end, more likely to deteriorate the cell performance. Increasing the interfacial strength between the particle and SE can suppress the interface debonding but induces high stress (up to 10 GPa). Results reveal the underlying mechanism of the electrochemical-mechanical coupling failure mechanism for composite cathode and provide promising guidance on the further improvement of a more robust composite cathode for ASSBs.

Keywords: All-solid-state battery; Composite cathode; Interfacial instability; Failure; Electrochemical-mechanical coupling

1 Introduction

All-solid-state batteries (ASSBs) are considered promising candidates for next-generation batteries due to their excellent safety performance guaranteed by inorganic solid electrolytes (SEs) with the non-flammability nature as well as the doubled energy density (~400 Wh/kg) enabled by the adoption of lithium metal anode.[1-3] The critical issue to be addressed for the commercialization of ASSBs involves interfacial instability.[4,5] Different from the conventional lithium-ion batteries (LIBs) using liquid electrolytes, all the components within ASSBs system, including the cathode, anode, and electrolyte, are solid-state. All the interfacial contact within ASSBs is solid-to-solid type, i.e., electrode-electrolyte interface and lithium dendrite-electrolyte interface.[4,6] As such, mechanical interfacial instability problems emerge. Mechanical instabilities at the solid-solid interface are one of the major reasons to cause the capacity fade, resistance increase, and soft internal short circuit, hindering the commercial application of the ASSBs.[6-8] The dendrite-electrolyte interface issues have been widely explored by the experiment and numerical methods,[9-12] and various strategies are proposed to solve the lithium penetration-induced short circuit problem.[13-15]

Recently, the design concept of composite cathodes with both active particles and solid electrolytes has been introduced where particles are mixed with SEs,[16-19] to offer a high specific contact area, reduce internal resistance, and enlarge the areal loadings for ASSBs. However, the repeated particle volume expansion/shrinkage during battery charging-discharging cycles may cause interface instability in the particle-electrolyte interface. The Young's modulus of inorganic ceramic-type SEs is usually above 10 GPa,[6] or even 150 GPa for $Li_7La_3Zr_2O_{12}$ (LLZO)

electrolyte,[20] which serves as a strong constraint of particle volume variation. The mismatching between large volume change (up to 8%) of common layered cathode compounds [21,22], and limited deformation of solid electrolyte [23] leads to the large and nonlinear deformation, plastic deformation, cracks of cathode particles, and interfacial debonding between cathode active particles and solid electrolyte. The interfacial debonding was found to be the main cause of the battery performance deterioration and safety problems due to the above-mentioned mechanistic behaviors.[24] The liquid electrolyte counterpart also shows the particle crack, but the electrolyte can infiltrate into the cracked region and the electrochemically active area increases consequently.[25]

Pioneering research work has touched upon the evolution of cathode microstructure and interfacial debonding in the composite cathode. Most of the work relies on the advanced characterization of specific charging/discharging-induced mechanical behaviors in ASSBs.[24,26-28] A gap was observed between the $LiNi_{0.8}Co_{0.1}Mn_{0.1}O_2$ (NCM811) active particle and β-Li_3PS_4 sulfide-based SE after fifty charging/discharging cycles by SEM, leading to the increased interfacial resistance and capacity loss.[27] The X-ray computed tomography (CT) was employed to characterize the delamination of the β-Li_3PS_4 SE from the $LiNi_{0.6}Mn_{0.2}Co_{0.2}O_2$ (NCM622) active particle surface in the composite cathode.[28] The focused ion beam scanning electron microscope (FIB-SEM)-based tomography further revealed severe mechanical degradation of ASSB composite cathode.[24] A large void volume (9.50%) was observed near the cathode particle surfaces, leading to a contact area loss of more than 10%. The chemo-mechanical breakdown of composite electrodes is localized heterogeneously [29]. Moreover, the cracks were discovered to initiate and develop inside the secondary NCM particles,[25,30] and $LiNi_{0.80}Co_{0.16}Al_{0.04}O_2$ (NCA) particles,[31]

demonstrating the chemo-mechanical instability induced bulk damage of the particles within the composite cathode, which was found to be caused by the polycrystalline structure [32,33]. Furthermore, heterogeneity of mesoscale local redox reaction in the NCM811 cathode particles was revealed by the nano-resolution synchrotron spectro-microscopy [34], and the local compositional heterogeneity of the polycrystalline NCM particle influences the global structural and electrochemical properties [35].

Current experimental characterizations provide a basic idea of mechanical instability problems in the composite cathode. Due to the spatial and temporal limitations, quantitative relations between mechanical damage and electrochemical performance deterioration are difficult to establish via *in-situ*/*operando* characterizations. Thus, physics-based multiphysics models are in pressing need to understand the quantitative mechanism[36-38]. To quantitatively study the effect of the contact area loss on the cyclic performance, the imperfect contact was incorporated into a 1D Newman battery model, revealing the faster drop of discharging voltage and capacity at a higher rate.[39] Newman battery model was developed based on the physical equations and widely adopted to describe the physiochemical phenomena inside the batteries, including the Li diffusion in active materials, ion transport in the electrolyte, and charge-transfer reactions at the electrode-electrolyte interface.[40] Further, the mechanical damage initiation and evolution of the composite electrode in ASSB induced by intercalation expansion were studied by a coupled electro-chemo-mechanical model using the cohesive zone method,[41] showing that fracture was prevented when the active particle's expansion was below 7.5%. The meso-scale simulation of interconnected particles in SEs demonstrated the inside stress distribution and found that smaller particles could improve rate

performance and avoid interfacial failure. A 3D microstructure-resolved model of the composite electrode was established based on the X-ray phase contrast tomography data to simulate the mechanical degradation in the composite electrode.[42] However, due to the highly multiphysics-coupled nature, the absence of understanding of the mechanical-electrochemical coupling mechanism for the fatal interfacial debonding and particle cracking issues poses challenges to accurately describing the performance degradation of ASSBs caused by the composite cathode.

To this end, the 3D electrochemical-mechanical coupled model is developed in this study, considering the complicated heterogeneous particle structure, as well as battery electrochemical kinetics, Li diffusion process, mechanical deformation, and interface debonding, to obtain an in-depth understanding of the failure behaviors inside the composite cathode of ASSBs. The quantitative results from the established model give out insights into the mechanisms of interfacial debonding and particle bulk damage, which further result in the degradation of the cell performance. The governing effects from charging rates (C-rates), heterogeneous properties, interfacial strength, and particle position are then comprehensively investigated to provide possible solutions to improve the robustness of composite cathodes in ASSBs.

2 Results

To investigate the coupled electrochemical-mechanical behavior inside the composite cathode of ASSBs, the 3D representative region, including the composite cathode, LLZO electrolyte, and lithium anode surface, is selected as the target domain in this study (Figure 1). The composite cathode comprises the $LiNi_{1/3}Co_{1/3}Mn_{1/3}O_2$ (NCM111) secondary particle, electrolyte-carbon

black domain (ECBD). The area capacity of the composite cathode used in this model is 0.295 mAh/cm^2. The initial state of the composite cathode is assumed to be the beginning of charging without any initial damage or defects. ECBD is the electronic-ionic conductive mixture of LLZO SE and carbon black, where the LLZO provides the ion transport path and the carbon black is the electronic conductive additive. The Li ions move between the NCM111 particle and the lithium anode, and the electrons moves between the cathode current collector and the particle surface to participate in the charge-transfer reaction. LLZO is in a polycrystalline structure and the carbon black is added as the particle. One target of this study is on the electrochemical-mechanical coupling failure mechanism of active particle with polycrystalline structure, and here we choose NCM111 particle as the specific polycrystalline case to demonstrate the general failure mechanism which is applicable to similar scenarios with higher Ni content. The stress developed inside the uniformly-structured single-crystal particle is unlikely to cause particle fracture, and we only focus on polycrystalline particle. The secondary particle consists of 53 primary particles ranging from 0.1 to 3 μm with shapes and crystallographic directions randomly generated through Voronoi tessellation. The volume change and lithium diffusivity along different directions in the primary particles are anisotropic and determined by the crystallographic directions. The radius of the secondary particle is 5 μm. LLZO and carbon black ratios in ECBD determine the effective electrical and ionic conductivity, directly affecting the electrochemical performance at the cell level. Furthermore, the structure of LLZO and carbon black, such as the crystal orientation, size, and polycrystalline structure, will finally influence the structure and morphology of ECBD, which may potentially impact the particle-ECBD interfacial failure and needs more efforts in future work.

Since this study focuses on the failure mechanism of the composite cathode, especially on the particle-related phenomena, the ECBD and electrolyte domain (ED) are simplified as homogenized regions with effective properties in the model, and the parameters of particle size, porosity, and carbon/binder content, are defined as constants, and their effects are not further discussed in this study. We develop a 3D electrochemical-mechanical coupled model to investigate the failure behavior of the composite cathode in ASSBs (Methodology section, Supplementary materials). There is no gap in the initial contact between the NCM particle and its surrounding ECBD, i.e., the particle surface is in contact with the ECBD surface without any gap at the charging beginning. We firstly establish the one-dimensional (1D) battery model with NCM111 cathode, LLZO solid electrolyte and lithium anode (Figure S1), and the predicted 0.1C charging/discharging potential (NCM111 vs. Li/Li^+) vs. specific capacity curves by the 1D model agree well with the experiment results in a voltage window of 3.0–4.3 V vs. Li/Li^+ at 25 °C (Figure S1),[18] which verifies the electrochemical parameters employed in the 3D model in Figure 1. This validated modeling framework further investigates the electrochemical-mechanical coupling failure mechanism.

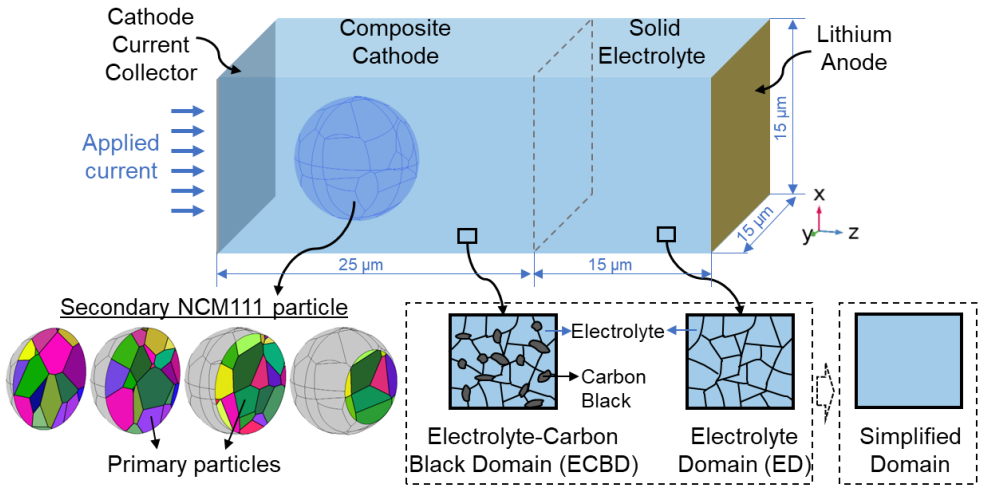

Figure 1. Illustration of the established 3D model consisting of a composite cathode (NCM111 secondary particle, electrolyte-carbon black domain (ECBD)), LLZO solid electrolyte domain (ED), and a lithium anode. The ECBD and the ED are simplified as the homogenized domains with effective conductivity and diffusivity. The modeling size is indicated in the figure. The external charging/discharging current is applied to the left boundary. The periodic boundary condition is adopted for the four side surfaces, and the left boundary is mechanically fixed.

To obtain a basic understanding of the typical failure phenomena in the composite cathode, we first focus on the scenario of the cell, including one NCM111 secondary particle in the cathode domain (Figure 1) at 1C constant-current (CC) charging and CC discharging scenario. The lower and upper cut-off voltages are 3 V and 4.3 V, respectively. Compared to the solid-electrolyte battery, the NCM particle-electrolyte interfacial debonding gap is much smaller and the particle-domain stress is also lower in the liquid-electrolyte battery (by only substituting the electrolyte while keeping the anode and cathode unchanged, Figure S2), indicating that the electrochemistry-mechanics coupled damage is more severe in the composite cathode of ASSBs. Since our focus is on the representative region with only one particle and the initial interfacial contact is assumed perfect, the interfacial debonding caused voltage response variation is not significant for ASSB compared to its liquid-electrolyte counterpart. In terms of the solid-electrolyte scenario, the total charging and discharging times are 3103 s and 3008 s, respectively (Figure 2A), with a Coulomb

efficiency (CE) of 96.94% (discharging time/charging time), indicating the capacity loss caused by the internal impedance going on inside the cell. The effect from the interfacial side reactions is not included in this study. During the charging process, the NCM active particle shrinks to cause the particle-electrolyte interface debonding, further increasing the interfacial impedance increases and hindering the electrochemical reaction, which adversely affects battery capacity retention. This study focuses mainly on the composite cathode failure mechanism from two aspects, i.e., (i) the interfacial failure between the cathode particle and its surrounding ECBD, and (ii) the bulk damage inside the cathode particle.

As for the interfacial failure between particle and ECBD, the concern is mainly with the interface debonding issue. Upon charging, delithiation occurs within the NCM111 particle, whose overall volumetric strain is negative[43], i.e., the volume of the NCM111 particle shrinks during delithiation (Figure S3A). Meanwhile, the LLZO solid electrolyte owns Young's modulus of 150 GPa, representing a strong stiffness to resist deformation. As a result, the interface between the particle and its surrounding ECBD begins to separate (Figure 2B) once the onset criterion of the interfacial debonding is fulfilled (Equation 17, Supplementary materials). Here the average interfacial debonding gap D_{G_ave} (overall debonding) and maximum gap D_{G_max} (worst-scenario debonding) are adopted to quantitatively characterize the progressive failure process at the particle-ECBD interface (Figure 2B). D_{G_ave} and D_{G_max} both gradually increase until t=2200 s to D_{G_ave}=0.3 nm and D_{G_max}=6.8 nm, then rapidly increase to their maximum values D_{G_ave}=14.3 nm and D_{G_max}=55 nm, respectively, at charging end (t=3103 s). Such behaviors significantly raise the interfacial impedance, and the charge transfer is restrained once the interface is detached. To

quantitatively characterize the interface debonding effect, the interfacial electrical resistance R_{int} considered in the model is exponentially related to the debonding gap (Figure S3B) at each particle surface point (similar to interfacial contact area around the whole particle surface). The increased R_{int} will cause a higher charging voltage to reach the upper cut-off voltage earlier, resulting in a smaller charging capacity acceptance of the cell. Meanwhile, higher R_{int} induces a larger overpotential at the particle-ECBD interface (Equation 2, Supplementary materials) to slow down the electrochemical reaction kinetics. Around the charging end and discharging beginning (t=3100~3350 s), D_{G_ave} and D_{G_max} remain at a high-value plateau because the maximum volumetric strain (Figure 2C) and the volume change of the whole particle (Figure S3A) reach a plateau which directly determines the corresponding debonding gap. After t=3350 s, the lithiation induces the particle volume expansion, then the debonding gap decreases, and the interfacial contact gradually recovers (Figure 2B). The interfacial resistance exists and acts continuously during the CC discharging, possibly causing the capacity loss and the above-mentioned 96.94% CE. Furthermore, at the discharging end, the debonding gap is not completely recovered (D_{G_ave}=0.255 nm and D_{G_max}=0.889 nm), which may further accumulate in long-time cycling to contribute to the performance degradation.

The applied external pressure to ASSB cells was reported to improve the interfacial contact between solid components inside ASSBs.[44] The external pressure applied to ASSB during operation (i.e., charging/discharging) is normally at MPa level,[45] as too large external pressure is likely to drive Li creeping through the electrolyte to mechanically short the cell.[46] Here we select external pressure P_{ext}=0, 5, 10, and 15 MPa, to study its effect on the particle-electrolyte debonding

gap during charging process. P_{ext} is applied to the left side and the right boundary is fixed (Figure S4A). With increasing P_{ext}, the average debonding gap D_{G_ave} is reduced, i.e., D_{G_ave}=14.3, 12.8, 12.5, 12.2 nm for P_{ext}=0, 5, 10, 15 MPa at charging end, respectively (Figure S4B). This clearly shows that the external pressure can improve the particle-electrolyte interface contact. While such improvement is limited and the remaining debonding gap is still large, and it further indicates that the debonding behavior is mainly dominated by the internal factors. Thus, the target of this study is on the internal electrochemical-mechanical coupling mechanism of particle-electrolyte interaction, and the external pressure effect is not included in the following section.

The failure inside the NCM secondary particle comes down to cracking or pulverization issues. The principal stress is the normal stress acting on the principal plane, while von Mises stress σ_{Mises} adopted here usually determines the yield or fracture of a given material, so σ_{Mises} is selected to describe the stress effect on particle damage. Once the energy release rate exceeds the fracture toughness (~0.1MPa $m^{1/2}$ for NCM [47]), then crack will occur inside the NCM particle. The energy release rate reaches its peak value at the region with large concentrated stress/strain, which is most likely to cause the particle fracture. The maximum von Mises stress σ_{Mises_max} within the particle domain increases during the CC charging process from initial stress-free status to σ_{Mises_max}=2.64 GPa at t=3103 s (Figure 2C). The generated stress results from the lithiation/delithiation-induced deformation and the constraint from the surrounding ECBD. Such a large stress probably causes the cracking failure of the particle. At the charging end (t=3103 s), the stress is mainly concentrated around and inside the particle domain, and the region away from the particle remains at a low-stress status (the 3D profiles of von Mises stress σ_{Mises} of the whole cell (Figure 2D)). To look

further at the phenomena occurring inside the secondary particle, we cut three 2D cross sections from the 3D geometry, *i.e.*, X-Y, Z-Y, and Z-X planes. Surprisingly, σ_{Mises} distributes nonuniformly in all the cross sections, especially at the boundaries of the primary particles (Figure 2D). The Z-Y profiles of the governing variables (namely, Li concentration c, volumetric strain ε_{V}, and von Mises stress σ_{Mises}) at specific times are collected to understand the overall evolution process during battery operation, including the charging/discharging start, middle, and end times (*i.e.*, t=0, 1550, 3103, 4650, 6111 s). In the beginning, the particle is at a free-stress/strain state with uniform initial concentration distribution (t=0 s, Figures 2E-G). During the charging process (along with delithiation of NCM particle), the concentration c decreases throughout the particle, simultaneously showing the overall trend of smaller c closer to the particle surface (t=1550 s, Figure 2E) because charge transfer reaction occurs at the particle-ECBD interface. However, c evolves nonuniformly caused of the randomly distributed primary particles with different crystallographic orientations. Since both the diffusivity and expansion coefficients vary along the [100], [010], and [001] directions, the overall Li diffusion and volume change are anisotropic for the secondary particle. Such anisotropy eventually leads to the significant nonuniformity of c and ε_{V} (t=1550 s, Figures 2E-F). Though the overall volumetric strain is negative for NCM secondary particle during charging (*i.e.*, secondary particle volume shrinks), the delithiation-induced strains are negative along [100] and [010] directions (volume contraction) while positive along [001] direction (volume expansion). Such a mismatch of volume change further aggravates the nonuniformity of the strain (Figure 2F) and lead to the nonuniform stress profiles (Figure 2G). The maximum stress and strain increase, and the stress/strain fields become more inhomogeneous

during charging, especially at the boundaries of the small primary particles (t=3103 s, Figures 2F-G). Observed cracks inside NCM secondary particles [30,31,33] are the mechanical failure consequence due to the weaker grain boundary connections between primary particles compared to particle bulk domains. During the discharging process, the lithiation leads to a larger c closer to the secondary particle surface (t=4650 s and 6111 s, Figure 2E). The nonuniform c and the inhomogeneous volume change of the primary particles (expansion along [100], [010] directions, contraction along [001] direction) cause the nonuniformity of strain and stress distribution (t=4650 s and 6111 s, Figures 2F-G). Interestingly, at discharging end, the Li concentration is not recovered to its initial state such that there are residual stress and strain within the particles. This serves as a partially responsible reason for the above-mentioned 96.94% CE and may also accumulate during the cycling to further degrade the cell performance. There may be interfacial side reactions between specific types of active particle and solid electrolyte.[48] The side reaction may cause additional localized volumetric strains to accelerate the pulverization of the secondary particles,[49] which needs further investigation in future research, and the focus of this study is on the particle crack caused by the nonuniform stress inside the polycrystalline particle.

In short, both interfacial debonding failure at the particle-ECBD interface and the cracking failure inside the particle is the results of electrochemistry-mechanics interactions, mainly from three aspects: (1) delithiation-induced NCM particle volume contraction under the constraint by the surrounding stiff ECBD; (2) structural inhomogeneity caused by the randomly distributed crystallographic orientations of the primary particles with anisotropic Li diffusion; (3) nonuniform Li concentration and volume variation mismatch-caused concentrated stress around the boundaries

of primary particles. We will further discuss the effects of various governing factors based on this model, *i.e.*, the charging rate, heterogeneity, interfacial strength, and particle position, to understand the underlying electrochemical-mechanical coupled mechanism fully.

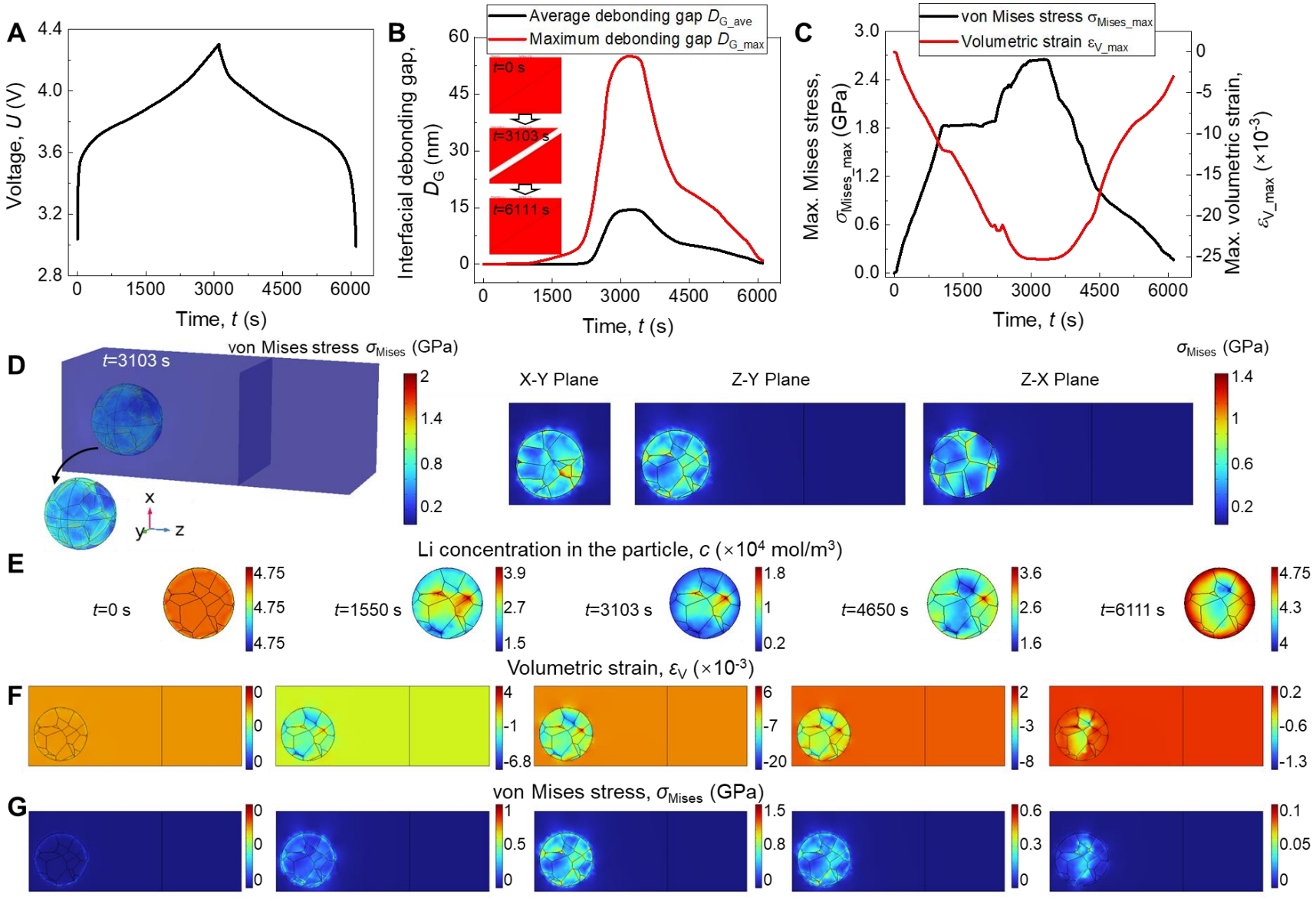
A
Voltage, U (V)
Time, t (s)
B
Average debonding gap D_G_ave
Maximum debonding gap D_G_max
t=0 s
t=3103 s
t=6111 s
Interfacial debonding gap, D_G (nm)
Time, t (s)
C
von Mises stress σ_Mises_max
Volumetric strain ε_V_max
Max. Mises stress, σ_Mises_max (GPa)
Max. volumetric strain, ε_V_max (×10^-3)
Time, t (s)
D
t=3103 s
von Mises stress σ_Mises (GPa)
X-Y Plane
Z-Y Plane
Z-X Plane
σ_Mises (GPa)
E
Li concentration in the particle, c (×10^4 mol/m^3)
t=0 s
t=1550 s
t=3103 s
t=4650 s
t=6111 s
F
Volumetric strain, ε_V (×10^-3)
G
von Mises stress, σ_Mises (GPa)

Figure 2. Electrochemical-mechanical coupled behavior of the composite cathode.
(A) Cell charging/discharging voltage curve.
(B) The average and the maximum debonding gap at the particle-electrolyte interface, $D_{G\_ave,}$ and D_{G_max}.
(C) The maximum von Mises stress σ_{Mises_max} and maximum volumetric strain ε_{V_max} (negative value due to volume shrinkage) of the particle during charging/discharging.
(D) The von Mises stress σ_{Mises} of the 3D cell and its cross sections at X-Y, Z-Y, Z-X planes.
The contour plots of various variables at different times, including t=0 s (charging beginning), 1550 s (charging midpoint), 3103 s (charging end), 4650 s (discharging midpoint), and 6111 s (discharging end): (E) Li concentration in the particle c, (F) volumetric strain ε_V, and (G) von Mises stress σ_{Mises}.

3 Discussion

3.1 Charging rate effect

Achieving high charging rates (C-rates) is one of the main limiting factors for the commercialization of the current ASSBs, due to the severe mechanical instability and dendritic issues at large applied current densities. C-rates ranging from 0.1C, 0.5C, 1C to 2C are selected here. To fairly compare the results at different time scales from various C-rates, the actual time t is normalized by the nominal charging time t_0 at each C-rate, namely t_0=36000 s, 7200 s, 3600 s, and 1800 s for 0.1C, 0.5C, 1C, and 2C, respectively. The CC charging-CC discharging scenario is discussed here, and the scenario with constant-voltage (CV) charging is included in the supplementary materials.

The cell at a higher C-rate shows a smaller charging/discharging capacity (Figure 3A), usually attributed to the larger interfacial polarization and larger voltage drop caused by internal resistance. However, the underlying reason is that the increased impedance leads to Li stored in the NCM secondary particle less diffused to the anode at higher C rates (Figure 3B). With the help of the established model, the total amount of Li M_{Li} is calculated by integral of the Li concentration c within the secondary particle domain, and M_{Li} decreases during charging due to the delithiation

and vice versa for discharging (Figure 3B). For the secondary particle, the initial M_{Li}=24.659×10^{-12} mol at t=0 s decreases to M_{Li}=1.666×10^{-12}, 2.362×10^{-12}, 3.203×10^{-12}, and 4.615×10^{-12} mol at the charging end for 0.1C, 0.5C, 1C, and 2C, respectively, which serves as the direct evidence that more Li remains within the NCM particle without participating the charge transfer reaction at a higher C-rate, thus the charging capacity is reduced. The concentration c that directly indicates the delithiation state determines the volumetric strain ε_V (Figure 3C) and the corresponding deformation (namely, particle volume change, Figure S5) where the volume of the particle shrinks during charging, resulting in increased stress σ_{Mises} inside the particle (Figure 3D). Note that the peak values of maximum ε_V and σ_{Mises} are very close for all the C-rates, *i.e.*, ε_{V_max}=-0.0253 and σ_{Mises_max}=2.64 GPa, since they all reach the plateau stage. The occurrence of the plateau stage in the ε_{V_max}, σ_{Mises_max}, and D_G is caused by the opposite volume change along [001] direction to counteract the volume change along [100] and [010] directions. Nevertheless, the particle at high C-rates exhibits a less contracted volume (Figure S5) due to higher resided Li within the particle, especially in the 2C case. Thus the peak values of the maximum and average debonding gaps of the particle-ECBD interface are smaller at 2C at the charging end, *i.e.*, D_{G_ave}=13.5 nm and D_{G_max}=52.5 nm, compared to D_{G_ave}=14.3 nm and D_{G_max}=55 nm at 1C (Figures 3E-F).

The higher C-rate appears to contribute less to the interfacial failure and bulk damage during the charging process, evaluated by D_G and σ_{Mises}, respectively, whereas the situation is completely reversed once the discharging process is included. During the discharging (lithiation of NCM particle), the Li amount M_{Li} in the particle increases, and correspondingly, the other main state variables (i.e., ε_V, σ_{Mises}, D_{G_ave}, and D_{G_max}) gradually recover. However, these variables cannot

completely recover by the end of discharging (Figures 3B-F). The total Li amount M_{Li}=24.518×10^{-12}, 24.058×10^{-12}, 23.647×10^{-12}, and 22.772×10^{-12} mol at the discharging end for 0.1C, 0.5C, 1C, and 2C, respectively, are lower than the initial M_{Li}=24.659×10^{-12} mol at t=0 s, which also indicates that M_{Li} at a higher C-rate shows a larger residual discrepancy to the fully recovered state (Figure 3B). Consequently, at the discharging end, the maximum volumetric strain and von Mises stress have larger residual values at higher C-rates, i.e., ε_{V_max}=-0.0398×10^{-3}, -0.835×10^{-3}, -3.032×10^{-3}, -5.891×10^{-3}, and σ_{Mises_max}=0.003, 0.048, 0.166, and 0.327 GPa for 0.1C, 0.5C, 1C, and 2C, respectively (Figures 3C-D). Some fluctuations in the curves are from the unstable volume expansion/contraction of the particle. Possible damage to the bulk particle could be caused by the residual ε_V and σ_{Mises}, especially at high C-rates with larger residual stress/strain, which may also be further accumulated after long-term cycling. Such progressive damage finally leads to the crack or pulverization of the particle. Furthermore, the particle volume at discharging end cannot be restored to its original state of good interfacial contact with the surrounding ECBD (Figure S5), and the unrecovered interface debonding gap after the CC discharging is larger at higher C-rates, *i.e.*, D_{G_ave}=0.01, 0.052, 0.255, 0.762 nm and D_{G_max}=0.036, 0.181, 0.889, 2.688nm for 0.1C, 0.5C, 1C, and 2C, respectively (Figures 3E-F), indicating larger interfacial impedance at higher C-rates, which could partially contribute to the deteriorated performance at higher C-rates. The cell at higher C-rates shows a worse interfacial contact and larger residual stress/strain within bulk particles after CC charging and discharging, which may be alleviated by adding the CV charging step but still cannot be completely recovered (Figure S6).

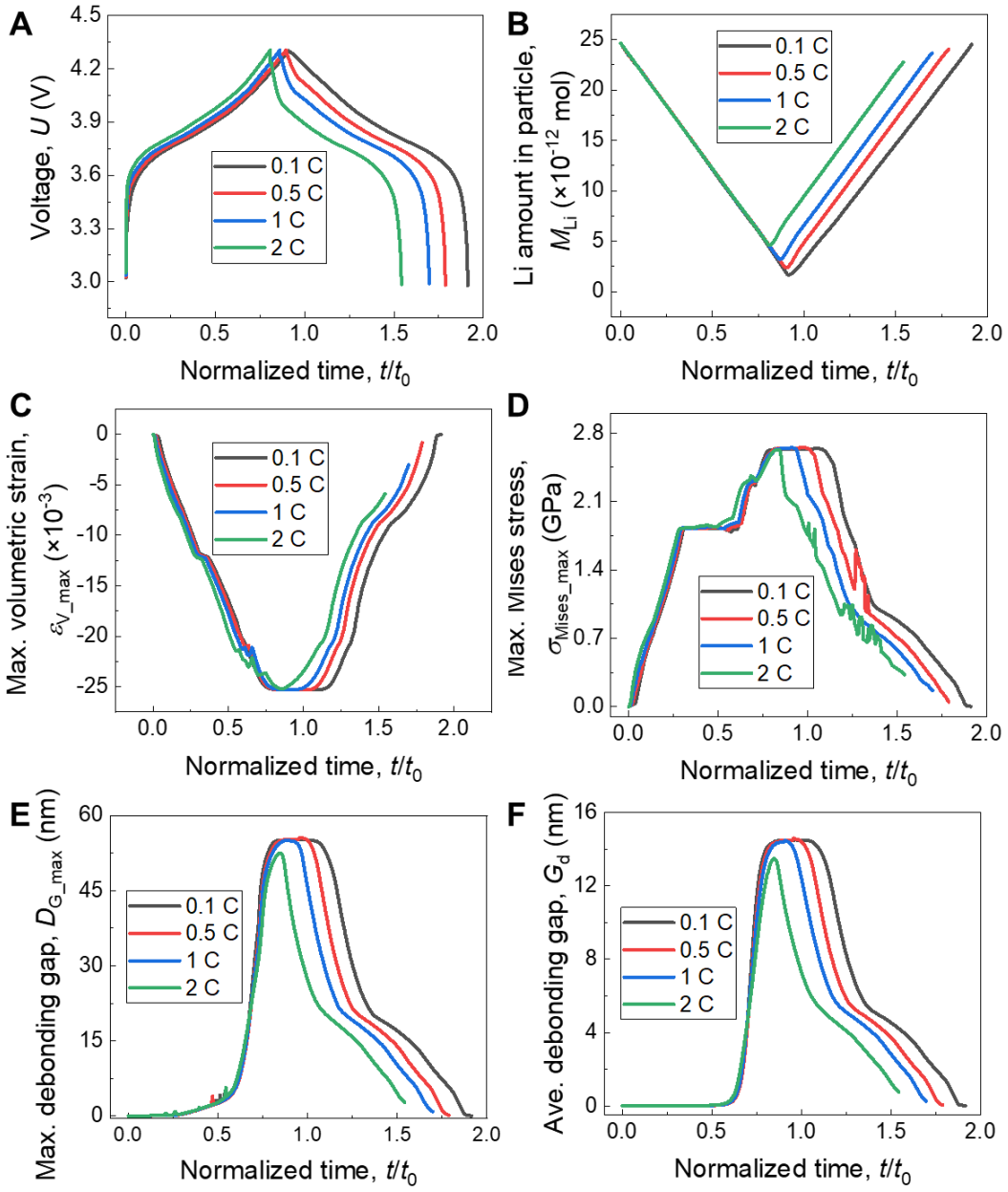

Figure 3. Effect of charging rate on the electrochemical-mechanical behavior of composite cathode in ASSBs.

(A) Cell charging/discharging voltage curves at different charging rates, i.e., C-rate=0.1C, 0.5C, 1C, and 2C.

(B) Li amount M_{Li} in the secondary NCM111 particle.

(C) Maximum volumetric strain of the particle ε_{V_max}.

(D) Maximum von Mises stress of the particle σ_{Mises_max}.

(E) Maximum particle-ECBD interfacial debonding gap D_{G_max}.

(F) Average particle-ECBD interfacial debonding gap D_{G_ave}.

Note that the time t is normalized by the nominal charging time t_0 (t_0=36000s, 7200s, 3600s, and 1800s for 0.1C, 0.5C, 1C and 2C, respectively).

3.2 Heterogeneity effect

The NCM secondary particle is a heterogeneous mixture composed of many randomly distributed primary particles with various sizes and crystallographic orientations. The orientation-determined Li diffusivity and expansion coefficient of primary particles lead to the significant heterogeneous distribution of the Li concentration, stress, and strain within the secondary particle (Figures 2E-F). The anisotropic diffusivity D_s (Equation 10, Supplementary materials) and anisotropic expansion coefficient matrix θ_β (Equation 16, Supplementary materials) are governing variables to define the anisotropy. In the baseline model, $D_{s11}=1\times10^{-14}$, $D_{s22}=1\times10^{-14}$, $D_{s33}=1\times10^{-20}$ m^2/s, and $\theta_{\beta11}=1$, $\theta_{\beta22}=1$, $\theta_{\beta33}=-1$ along [100], [010], [001] directions of each primary particle, respectively (*Case 1*). To further look into the heterogeneity effect, various cases with different D_s and θ_β are considered (Figure 4)--*Case 1*: baseline scenario; *Case 2*: isotropic D_s ($D_{sii}=1\times10^{-14}$ m^2/s (i=1, 2, 3)), and θ_β ($\theta_{\beta11}=\theta_{\beta22}=1$, $\theta_{\beta33}=-1$); *Case 3*: isotropic D_s, and θ_β ($\theta_{\beta11}=\theta_{\beta22}=1$, $\theta_{\beta33}=-0.5$); *Case 4*: isotropic D_s, and θ_β ($\theta_{\beta11}=\theta_{\beta22}=1$, $\theta_{\beta33}=0$). Specifically, *Case 1* and *2* are to explore the heterogeneity effect from diffusivity, and *Case 2*, *3*, and *4* are to study the heterogeneity effect from expansion. Note that 1C C-rate is selected for all the following discussions.

Switching Li diffusivity D_s from the anisotropic *Case 1* to isotropic *Case 2*, the cell charging/discharging time are both elongated from 3103 s/3008 s to 3185 s/3155 s (Figure 4A), due to the fact that the particle is more delithiated during charging and less Li remains at the charging end in *Case 2*, and more Li remains at the discharging end in *Case 1* (Figure 4B). The corresponding Coulomb efficiency is increased from 96.94% (*Case 1*) to 99.06% (*Case 2*), indicating that increasing D_s and reducing the diffusive anisotropy are beneficial for battery

performance improvement. Since the maximum volumetric strain and particle volume change during charging are close for *Case 1* and *2* (Figures S7A-B), the peak values of debonding gap D_{G_ave} and stress σ_{Mises_max} are also close (Figures 4C-D). However, the Li concentration shows a much greater nonuniformity in *Case 1* (Figure 4E). Moreover, at the discharging end, the residual Li amount in the particle ($\Delta M_{Li}=M_{Li,\ charging\ beginning} - M_{Li,\ discharging\ end}$) in anisotropic *Case 1* $\Delta M_{Li}=1.012\times10^{-12}$ mol is larger than that of isotropic *Case 2* $\Delta M_{Li}=0.744\times10^{-12}$ mol, caused by the slow diffusivity $D_{s33}=1\times10^{-20}$ m^2/s in *Case 1*. Larger ΔM_{Li} results in larger residual debonding gap and stress at the discharging end, namely, $D_{G\_ave}=0.255$ nm and $\sigma_{Mises\_max}=0.166$ GPa in *Case 1*, both larger than $D_{G\_ave}=0.092$ nm and $\sigma_{Mises\_max}=0.069$ GPa in *Case 2*. It implies that smaller and anisotropic D_s could also cause more mechanical damage to the particle and debonding issues in addition to capacity reduction.

The lithiation/delithiation-induced deformation along [001] direction of the NCM primary particle is opposite to other directions, as can be reflected by $\theta_{\beta11}=1$, $\theta_{\beta22}=1$, $\theta_{\beta33}=-1$ along [100], [010], [001] directions, respectively. Such deformation anisotropy causes the deformation mismatch of adjacent primary particles (Figure 2F) since their orientations are randomly generated and distributed. There are over 50 primary particles with random size and orientation inside the secondary particle, and it's rather difficult to keep the same volume change for each primary particles at different *Cases 1-4*. Greater stress heterogeneity generates inside the secondary particle and the stress mainly concentrates along the boundaries of primary particles can be observed (*Cases 1-2*, Figure 4F). *Cases 3* and *4* take $\theta_{\beta33}=-0.5$ and $\theta_{\beta33}=0$, respectively, which means less opposite deformation to the other two directions ($\theta_{\beta11}=\theta_{\beta22}=1$) compared to *Case 2* ($\theta_{\beta33}=-1$). The

deformation mismatch (*i.e.*, volumetric strain heterogeneity) in *Case 4* is significantly alleviated than in *Case 3*, also much better than *Case 2* (Figure S7D). Subsequently, the peak values of the von Mises stress and the stress distribution nonuniformity both follow *Case 4*<*Case 3*<*Case 2* (Figures 4D and 4F). Furthermore, due to the more uniform stress profile and thus less stress effect on Li diffusion (Equation 10, Supplementary materials), the Li concentration profile is more consistent in *Case 4* than in *Cases 3* and *2* (Figure 4E). Since the deformation along [001] direction is less expanded and more contracted for *Cases 3-4* than *Case 2* during the charging process, the particle volume at the charging end *Case 4*<*Case 3*<*Case 2* (Figure S7B) causes the interface debonding gap *Case 4*>*Case 3*>*Case 2* (Figure 4C). The larger interfacial resistance caused by the larger debonding gap results in a higher voltage drop across the interface (Figure S7C) and, thus shorter charging period of *Case 4* (Figure 4A). The volume variation in *Case 4* is the largest (Figure S7B), but the corresponding stress profile is the most uniform (Figure 4F), which is more intuitive to demonstrate the beneficial effect from more uniform expansion coefficient. To sum up, the less opposite and less anisotropic expansion coefficient will cause more uniform concentration, strain, and stress profiles demonstrating a less adverse effect on particle interior damage from a heterogeneous structure. In addition to modulating the expansion, minimizing particle volume variation is also essential to improve battery performance. This may serve as a promising way to improve the cyclability of the ASSB by controlling the crystallographic directions of primary particles to reduce the heterogeneity of the secondary particle.

Diffusion coefficient

$$D_s = \begin{bmatrix} 1\times10^{-14} & & \\ & 1\times10^{-14} & \\ & & 1\times10^{-20} \end{bmatrix} \mathrm{m^2/s}$$

Anisotropic

Expansion coefficient

$$\beta_c = \theta_\beta \beta_{c0}(c)/3 = \begin{bmatrix} 1 & & \\ & 1 & \\ & & -1 \end{bmatrix} \times \beta_{c0}(c)/3$$

Anisotropic

- ***Case 1***: anisotropic D_s, anisotropic θ_β (1 1 -1)
- ***Case 2***: isotropic D_s, anisotropic θ_β (1 1 -1)
- ***Case 3***: isotropic D_s, anisotropic θ_β (1 1 -0.5)
- ***Case 4***: isotropic D_s, anisotropic θ_β (1 1 0)

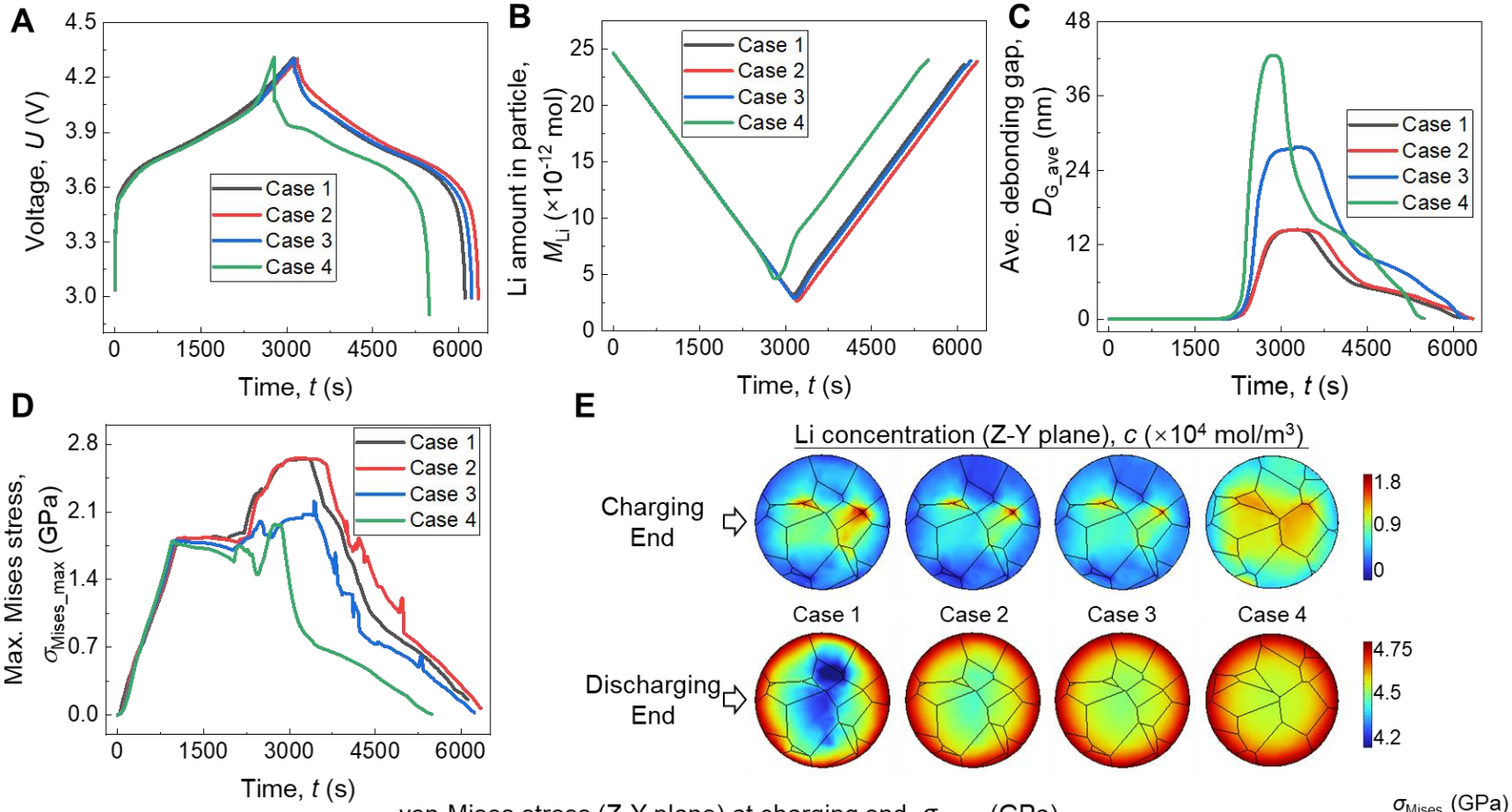

Figure 4. Effect of heterogeneity from diffusivity and expansion coefficient on the electrochemical-mechanical behavior of composite cathode in ASSBs.
(A) Cell charging/discharging voltage curves at different diffusion and expansion cases.
(B) Li amount M_{Li} in the NCM111 secondary particle.
(C) Average particle-ECBD interfacial debonding gap D_{G_ave}.
(D) Maximum von Mises stress of the particle σ_{Mises_max}.
(E) Li concentration c profiles of the Z-Y plane in the NCM111 secondary particle at the charging end and discharging end.
(F) von Mises stress σ_{Mises} profiles of the Z-Y plane at the charging end.

3.3 Interfacial strength effect

Interfacial modification or increasing the interfacial strength is a commonly adopted method to improve the interface contact between particles and surrounding electrolytes for better long-term cyclability performance. However, one question still remains to be answered: is stronger interfacial strength always beneficial for the composite cathode?

Herein various interfacial strength σ_c are selected as *Cases 1-4*, namely, σ_c=50, 100 (baseline)[42], 200, 500 MPa, and based on the same displacement, the corresponding fracture toughness G_c also varies (G_c=0.5, 1, 2, 5 J/m^2, for *Case 1-4*, respectively). Note that the strength is assumed to be the same in normal and shear directions.

The cell voltage shows little difference at different interfacial strengths in *Cases 1-4* (Figure 5A) due to the similar Li amount within the particle (Figure S8A). The interfacial strength serves as the mechanical constraint boundary condition for the deformation of the particle. Since stronger interfacial strength imposes a higher threshold value for the onset of interfacial separation/debonding, the interfacial debonding gap D_{G_ave} decreases with increasing σ_c (Figure 5B), and the D_{G_ave} peak values are 19.9, 14.3, 1.1, and 0.027 nm for σ_c=50, 100, 200, and 500

MPa, respectively. A similar trend also exists for D_{G_max} (Figure S8B). The debonding gap is nearly 0 at *Case 4* with high σ_c=500 MPa, indicating that increasing the interfacial strength to a certain value can address the interface debonding issue. The average voltage drop across the interface caused by the interfacial resistance is larger at lower σ_c. However, the maximum value is still small, below 0.015V (Figure S8A), which can also explain the close voltage responses in *Cases 1-4*. Since the higher σ_c constrains the volume shrinkage of the particle more strictly during charging, the volumetric strain ε_{V_max} gets larger to adapt to the particle contraction under the stronger constraint (Figure 5C), resulting in larger stress σ_{Mises_max} (Figure 5D). Both ε_{V_max} and σ_{Mises_max} peak values increase with σ_c, i.e., ε_{V_max}=-26×10^{-3}, -25.3×10^{-3}, -33.7×10^{-3}, -46.2×10^{-3}, and σ_{Mises_max}=2.1, 2.64, 3.86, 9.7 GPa for σ_c=50, 100, 200, 500 MPa, respectively. σ_{Mises} on the particle surface at certain points significantly increase with σ_c (Figure 5E), and σ_{Mises} inside the particle also develop an increasing trend (Figure 5F). The peak stress σ_{Mises_max} reaches above 9GPa at σ_c=500 MPa, most probably causing mechanical damage to the particle, such as crack or pulverization. Based on the above discussion, it is discovered that increasing the interfacial strength inside the composite cathode has competing contributions to the cell performance: suppressing the interface debonding to reduce interfacial impedance and inducing high stress to cause possible mechanical damage to the particle. Thus, controlling the particle volume variation and adopting appropriate interfacial strength may be a proper way to both ensure interfacial contact and avoid particle damage.

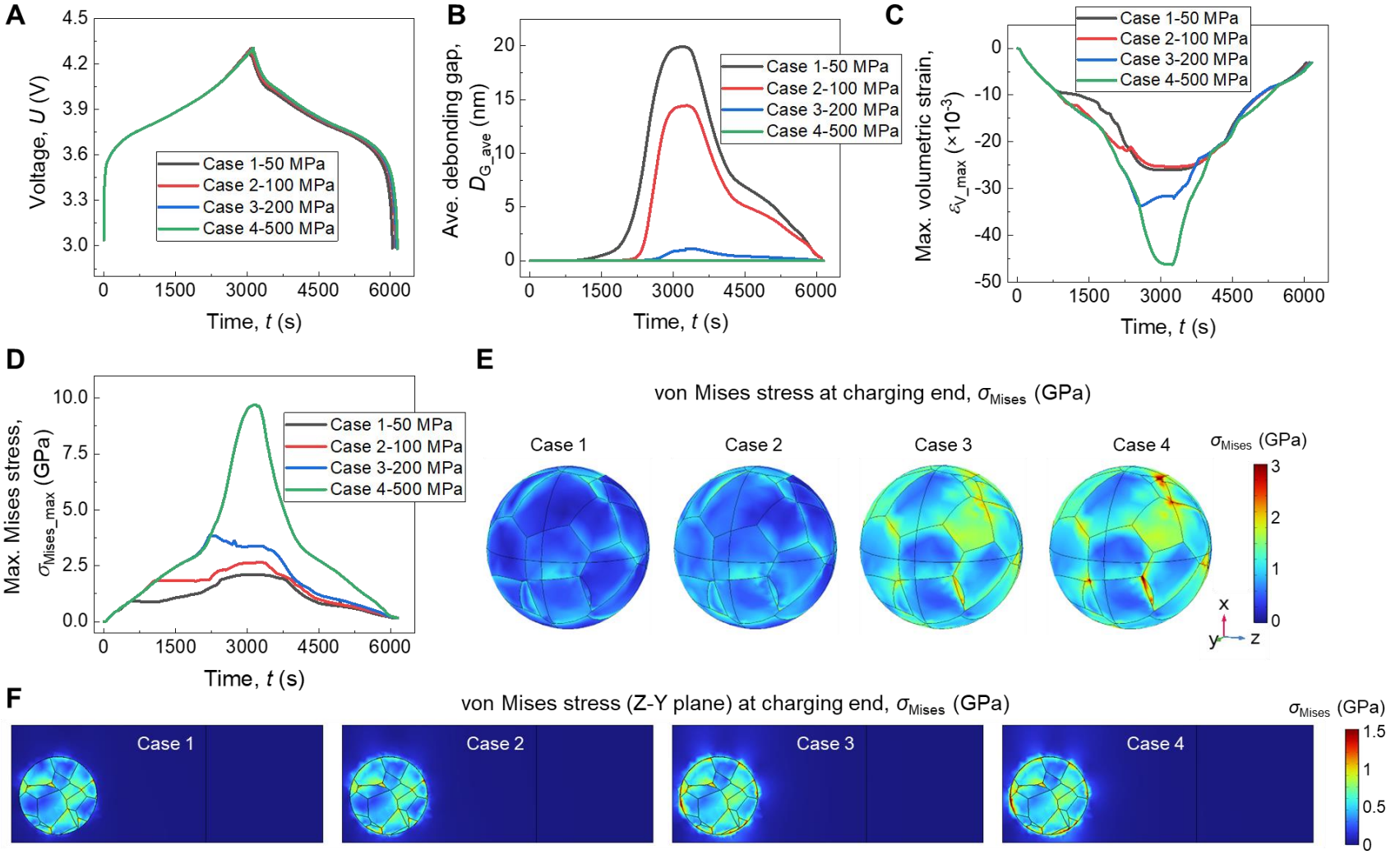
A
Voltage, U (V)
Time, t (s)
Case 1-50 MPa
Case 2-100 MPa
Case 3-200 MPa
Case 4-500 MPa
B
Ave. debonding gap, D_G_ave (nm)
Time, t (s)
C
Max. volumetric strain, ε_V_max (×10^-3)
Time, t (s)
D
Max. Mises stress, σ_Mises_max (GPa)
Time, t (s)
E
von Mises stress at charging end, σ_Mises (GPa)
Case 1
Case 2
Case 3
Case 4
σ_Mises (GPa)
F
von Mises stress (Z-Y plane) at charging end, σ_Mises (GPa)
Case 1
Case 2
Case 3
Case 4
σ_Mises (GPa)

Figure 5. Effect of interfacial debonding strength on the electrochemical-mechanical behavior of composite cathode in ASSBs.

(A) Cell charging/discharging voltage curves at different interface debonding strengths, *i.e.*, 50 MPa, 100 MPa, 200MPa, and 500MPa.

(B) Average particle-ECBD interfacial debonding gap D_{G_ave}.

(C) Maximum volumetric strain of the particle ε_{V_max}.

(D) Maximum von Mises stress for the particle σ_{Mises_max}.

(E) Von Mises stress σ_{Mises} profiles of the particle at the charging end.

(F) Von Mises stress σ_{Mises} profiles of the Z-Y plane at the charging end.

3.4 Particle position effect

The composite cathode in ASSBs contains numerous NCM secondary particles whose positions are randomly distributed in *x*, *y*, *z* directions. Usually, the active materials in the *x*-*y* plane are considered uniform at a fixed *z* value. Here the effect of particle position along the *z* direction on the electrochemical-mechanical behavior of composite cathode in ASSBs is investigated. Since the periodic boundary condition is applied to the side boundaries, asymmetry effect is trivial. Two particles are included, *i.e.*, P1 and P2 (Figure 6A). P1 is closer to the anode side while P2 is closer to the cathode current collector, and the *z*-axis distance between P1 and P2 is 12 μm. The stress mainly concentrates around or within the particle domain (Figure 6A).

During charging, the movement direction of Li ions is from the cathode particle to the anode side, and the NCM particle closer to the anode side will be firstly delithiated, evidenced by the lower Li amount in P1 at the beginning of the charging (Figure S9). Similarly, during discharging, the particle closer to the anode side is more lithiated, and P1 has a larger Li amount at discharging end than P2. The peak value of the maximum interfacial debonding gap D_{G_max} of P1 is 26.93 nm, larger than 26.66 nm of P2 (Figure 6B), indicating that the particle closer to the anode side suffers a worse interface debonding issue, especially in the thick-electrode design, while the interfacial

debonding condition may be close for different positions in the thin-electrode design. It also implies that a gradient design for the interfacial strength may be in need to make the particle interfacial durability the same through the thickness. Moreover, during the middle stage of the charging process (t=1200~2200 s), the maximum volumetric strain ε_{V_max} of P1 is about 2×10^{-3} larger than that of P2 (Figure 6C), which demonstrates more serious deformation in P1. Correspondingly, the maximum von Mises stress σ_{Mises_max} within P1 is also larger during this period (Figure 6D), indicating larger mechanical damage occurring in P1. The above results indicate the particle closer to the anode side suffers more severe interfacial debonding and bulk damage, which should be treated with enhanced properties during fabrication.

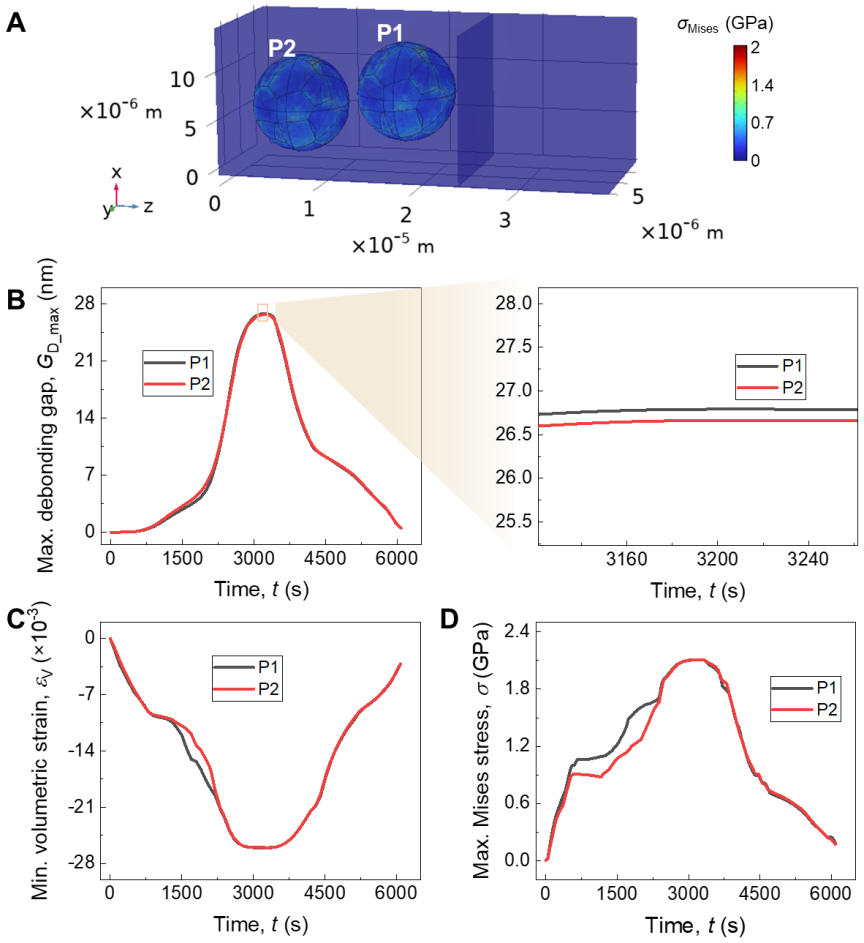

Figure 6. Effect of particle position on the electrochemical-mechanical behavior of composite cathode in ASSBs.
(A) Von Mises stress σ_{Mises} profiles of the cell at charging end.
(B) Maximum interfacial debonding gap D_{G_max}.
(C) Maximum volumetric strain of the particle ε_{V_max}.
(D) Maximum von Mises stress for the particle σ_{Mises_max}.

4 Conclusion

The failure issues inside the composite cathode of ASSBs are complicated multiphysics phenomena involving electrochemistry and mechanics, mainly demonstrated as particle damage and interfacial failure. Considering the electrochemical reaction kinetics, Li diffusion process, mechanical deformation, and interface debonding, the 3D electrochemical-mechanical coupled model is developed in this study to unravel the underlying failure mechanism. The randomly

distributed NCM111 primary particles inside the secondary particle result in the anisotropic Li diffusion and volume variation, which lead to significant nonuniformity of the Li concentration, strain, and stress profiles, especially along the boundaries of primary particles, finally causing the internal cracks or pulverization of the secondary particle. The NCM particle volume shrinks during charging while under the constraint of the surrounding stiff ECBD domain, gradually inducing the interface debonding and increasing the interfacial impedance to degrade cell capacity.

- Cells at larger C-rates show a smaller charging capacity and larger residual stress/strain/debonding gap at discharging end, thus more likely to deteriorate the performance, which may be partially improved by adding CV charging step.
- Furthermore, homogeneous Li diffusivity and expansion coefficient will cause more uniform concentration, strain, and stress profiles, thus mitigating the adverse effect of the heterogeneous structure.
- Increasing the interfacial strength between the particle and ECBD can suppress the interface debonding but also induce high stress to cause possible mechanical damage to the particle. Therefore, simultaneously controlling the particle volume variation and adopting appropriate interfacial strength may be a proper way to both ensure interfacial contact and avoid particle damage.
- Lastly, particle closer to the anode side suffers more severe interfacial debonding and bulk damage, which may be improved with enhanced properties during fabrication.

Results in this study provide a comprehensive understanding of the electrochemical-mechanical coupling failure mechanism inside composite cathode, shedding light on the further improvement of a more robust composite cathode for ASSBs from a design perspective.

Acknowledgment

Declaration of Interests

The authors declare no competing interests.

Author contribution

Data availability

The datasets used in this study are available from the corresponding author upon request.

References

1. Kato, Y., Hori, S., Saito, T., Suzuki, K., Hirayama, M., Mitsui, A., Yonemura, M., Iba, H., and Kanno, R. (2016). High-power all-solid-state batteries using sulfide superionic conductors. Nature Energy *1*, 16030. 10.1038/nenergy.2016.30.
2. Ye, L., and Li, X. (2021). A dynamic stability design strategy for lithium metal solid state batteries. Nature *593*, 218-222. 10.1038/s41586-021-03486-3.
3. Yao, X., Liu, D., Wang, C., Long, P., Peng, G., Hu, Y.-S., Li, H., Chen, L., and Xu, X. (2016). High-Energy All-Solid-State Lithium Batteries with Ultralong Cycle Life. Nano Lett *16*, 7148-7154. 10.1021/acs.nanolett.6b03448.
4. Wang, D., Zhu, C., Fu, Y., Sun, X., and Yang, Y. (2020). Interfaces in Garnet-Based All-Solid-State Lithium Batteries. Adv. Energy Mater. *10*, 2001318. 10.1002/aenm.202001318.
5. Lim, H.-D., Park, J.-H., Shin, H.-J., Jeong, J., Kim, J.T., Nam, K.-W., Jung, H.-G., and Chung, K.Y. (2020). A review of challenges and issues concerning interfaces for all-solid-state batteries. Energy Storage Mater. *25*, 224-250. 10.1016/j.ensm.2019.10.011.
6. Zhang, F., Huang, Q.-A., Tang, Z., Li, A., Shao, Q., Zhang, L., Li, X., and Zhang, J. (2020). A review of mechanics-related material damages in all-solid-state batteries: Mechanisms, performance impacts and mitigation strategies. Nano Energy *70*. 10.1016/j.nanoen.2020.104545.
7. Cao, D., Sun, X., Li, Q., Natan, A., Xiang, P., and Zhu, H. (2020). Lithium Dendrite in All-Solid-State Batteries: Growth Mechanisms, Suppression Strategies, and Characterizations. Matter *3*, 57-94. 10.1016/j.matt.2020.03.015.

8. Tang, Y., Zhang, L., Chen, J., Sun, H., Yang, T., Liu, Q., Huang, Q., Zhu, T., and Huang, J. (2021). Electro-chemo-mechanics of lithium in solid state lithium metal batteries. Energy Environ. Sci. 10.1039/d0ee02525a.
9. Hao, S., Daemi, S.R., Heenan, T.M.M., Du, W., Tan, C., Storm, M., Rau, C., Brett, D.J.L., and Shearing, P.R. (2021). Tracking lithium penetration in solid electrolytes in 3D by in-situ synchrotron X-ray computed tomography. Nano Energy *82*. 10.1016/j.nanoen.2021.105744.
10. Yuan, C., Gao, X., Jia, Y., Zhang, W., Wu, Q., and Xu, J. (2021). Coupled crack propagation and dendrite growth in solid electrolyte of all-solid-state battery. Nano Energy *86*. 10.1016/j.nanoen.2021.106057.
11. Yuan, C., Lu, W., and Xu, J. (2021). Unlocking the Electrochemical–Mechanical Coupling Behaviors of Dendrite Growth and Crack Propagation in All-Solid-State Batteries. Adv. Energy Mater. *11*, 2101807. 10.1002/aenm.202101807.
12. Yu, Z., Zhang, X., Fu, C., Wang, H., Chen, M., Yin, G., Huo, H., and Wang, J. (2021). Dendrites in Solid-State Batteries: Ion Transport Behavior, Advanced Characterization, and Interface Regulation. Adv. Energy Mater. *11*, 2003250. 10.1002/aenm.202003250.
13. Lu, Z., Yang, Z., Li, C., Wang, K., Han, J., Tong, P., Li, G., Vishnugopi, B.S., Mukherjee, P.P., Yang, C., and Li, W. (2021). Modulating Nanoinhomogeneity at Electrode–Solid Electrolyte Interfaces for Dendrite-Proof Solid-State Batteries and Long-Life Memristors. Adv. Energy Mater. *11*. 10.1002/aenm.202003811.
14. Yuan, C., Sheldon, B.W., and Xu, J. (2022). Heterogeneous Reinforcements to Mitigate Li Penetration through Solid Electrolytes in All-Solid-State Batteries. Adv. Energy Mater. 10.1002/aenm.202201804.
15. Lv, Q., Jiang, Y., Wang, B., Chen, Y., Jin, F., Wu, B., Ren, H., Zhang, N., Xu, R., Li, Y., et al. (2022). Suppressing lithium dendrites within inorganic solid-state electrolytes. Cell Rep. Phys. Sci. *3*. 10.1016/j.xcrp.2021.100706.
16. Kim, J.Y., Jung, S., Kang, S.H., Lee, M.J., Jin, D., Shin, D.O., Lee, Y.-G., and Lee, Y.M. (2022). All-solid-state hybrid electrode configuration for high-performance all-solid-state batteries: Comparative study with composite electrode and diffusion-dependent electrode. J Power Sources *518*, 230736. https://doi.org/10.1016/j.jpowsour.2021.230736.
17. Lou, S., Zhang, F., Fu, C., Chen, M., Ma, Y., Yin, G., and Wang, J. (2021). Interface Issues and Challenges in All-Solid-State Batteries: Lithium, Sodium, and Beyond. Adv Mater *33*, 2000721. https://doi.org/10.1002/adma.202000721.
18. Roitzheim, C., Sohn, Y.J., Kuo, L.-Y., Häuschen, G., Mann, M., Sebold, D., Finsterbusch, M., Kaghazchi, P., Guillon, O., and Fattakhova-Rohlfing, D. (2022). All-Solid-State Li Batteries with NCM–Garnet-Based Composite Cathodes: The Impact of NCM Composition on Material Compatibility. ACS Appl. Energy Mater. 10.1021/acsaem.2c00533.
19. Bielefeld, A., Weber, D.A., and Janek, J. (2018). Microstructural Modeling of Composite Cathodes for All-Solid-State Batteries. The Journal of Physical Chemistry C *123*, 1626-1634. 10.1021/acs.jpcc.8b11043.
20. Verma, A., Kawakami, H., Wada, H., Hirowatari, A., Ikeda, N., Mizuno, Y., Kotaka, T., Aotani, K., Tabuchi, Y., and Mukherjee, P.P. (2021). Microstructure and Pressure-Driven Electrodeposition Stability in Solid-State Batteries. Cell Rep. Phys. Sci. *2*. 10.1016/j.xcrp.2020.100301.
21. Kondrakov, A.O., Schmidt, A., Xu, J., Geßwein, H., Mönig, R., Hartmann, P., Sommer, H., Brezesinski, T., and Janek, J. (2017). Anisotropic Lattice Strain and Mechanical Degradation of High- and Low-Nickel NCM Cathode Materials for Li-Ion Batteries. The Journal of Physical Chemistry C *121*, 3286-3294. 10.1021/acs.jpcc.6b12885.

22. Weber, R., Fell, C.R., Dahn, J.R., and Hy, S. (2017). Operando X-ray Diffraction Study of Polycrystalline and Single-Crystal LixNi0.5Mn0.3Co0.2O2. J Electrochem Soc *164*, A2992-A2999. 10.1149/2.0441713jes.
23. McGrogan, F.P., Swamy, T., Bishop, S.R., Eggleton, E., Porz, L., Chen, X., Chiang, Y.-M., and Van Vliet, K.J. (2017). Compliant Yet Brittle Mechanical Behavior of Li2S–P2S5 Lithium-Ion-Conducting Solid Electrolyte. Advanced Energy Materials *7*, 1602011. https://doi.org/10.1002/aenm.201602011.
24. Shi, T., Zhang, Y.-Q., Tu, Q., Wang, Y., Scott, M.C., and Ceder, G. (2020). Characterization of mechanical degradation in an all-solid-state battery cathode. J. Mater. Chem. A *8*, 17399-17404. 10.1039/d0ta06985j.
25. Ruess, R., Schweidler, S., Hemmelmann, H., Conforto, G., Bielefeld, A., Weber, D.A., Sann, J., Elm, M.T., and Janek, J. (2020). Influence of NCM Particle Cracking on Kinetics of Lithium-Ion Batteries with Liquid or Solid Electrolyte. J. Electrochem. Soc. *167*. 10.1149/1945-7111/ab9a2c.
26. Liu, T., Zhang, Y., Chen, R., Zhao, S.-X., Lin, Y., Nan, C.-W., and Shen, Y. (2017). Non-successive degradation in bulk-type all-solid-state lithium battery with rigid interfacial contact. Electrochem Commun *79*, 1-4. https://doi.org/10.1016/j.elecom.2017.03.016.
27. Koerver, R., Aygün, I., Leichtweiß, T., Dietrich, C., Zhang, W., Binder, J.O., Hartmann, P., Zeier, W.G., and Janek, J. (2017). Capacity Fade in Solid-State Batteries: Interphase Formation and Chemomechanical Processes in Nickel-Rich Layered Oxide Cathodes and Lithium Thiophosphate Solid Electrolytes. Chem. Mater. *29*, 5574-5582. 10.1021/acs.chemmater.7b00931.
28. Neumann, A., Randau, S., Becker-Steinberger, K., Danner, T., Hein, S., Ning, Z., Marrow, J., Richter, F.H., Janek, J., and Latz, A. (2020). Analysis of Interfacial Effects in All-Solid-State Batteries with Thiophosphate Solid Electrolytes. ACS Applied Materials & Interfaces *12*, 9277-9291. 10.1021/acsami.9b21404.
29. Lin, F., Zhao, K., and Liu, Y. (2021). Heterogeneous Reaction Activities and Statistical Characteristics of Particle Cracking in Battery Electrodes. Acs Energy Lett. *6*, 4065-4070. 10.1021/acsenergylett.1c02135.
30. Ryu, H.-H., Park, K.-J., Yoon, C.S., and Sun, Y.-K. (2018). Capacity Fading of Ni-Rich Li[NixCoyMn1–x–y]O2 ($0.6 \leq x \leq 0.95$) Cathodes for High-Energy-Density Lithium-Ion Batteries: Bulk or Surface Degradation? Chem. Mater. *30*, 1155-1163. 10.1021/acs.chemmater.7b05269.
31. Jung, S.H., Kim, U.H., Kim, J.H., Jun, S., Yoon, C.S., Jung, Y.S., and Sun, Y.K. (2019). Ni-Rich Layered Cathode Materials with Electrochemo-Mechanically Compliant Microstructures for All-Solid-State Li Batteries. Adv. Energy Mater. *10*. 10.1002/aenm.201903360.
32. Xu, Z., Jiang, Z., Kuai, C., Xu, R., Qin, C., Zhang, Y., Rahman, M.M., Wei, C., Nordlund, D., Sun, C.J., et al. (2020). Charge distribution guided by grain crystallographic orientations in polycrystalline battery materials. Nat Commun *11*, 83. 10.1038/s41467-019-13884-x.
33. Lou, S., Liu, Q., Zhang, F., Liu, Q., Yu, Z., Mu, T., Zhao, Y., Borovilas, J., Chen, Y., Ge, M., et al. (2020). Insights into interfacial effect and local lithium-ion transport in polycrystalline cathodes of solid-state batteries. Nat Commun *11*, 5700. 10.1038/s41467-020-19528-9.
34. Qian, G., Zhang, J., Chu, S.-Q., Li, J., Zhang, K., Yuan, Q., Ma, Z.-F., Pianetta, P., Li, L., Jung, K., and Liu, Y. (2021). Understanding the Mesoscale Degradation in Nickel-Rich Cathode Materials through Machine-Learning-Revealed Strain–Redox Decoupling. Acs Energy Lett. *6*, 687-693. 10.1021/acsenergylett.0c02699.
35. Mu, L., Zhang, J., Xu, Y., Wei, C., Rahman, M.M., Nordlund, D., Liu, Y., and Lin, F. (2022). Resolving Charge Distribution for Compositionally Heterogeneous Battery Cathode Materials. Nano Lett *22*, 1278-1286. 10.1021/acs.nanolett.1c04464.

36. Wang, P., Qu, W., Song, W.-L., Chen, H., Chen, R., and Fang, D. (2019). Electro–Chemo–Mechanical Issues at the Interfaces in Solid-State Lithium Metal Batteries. Adv Funct Mater *29*, 1900950. https://doi.org/10.1002/adfm.201900950.
37. Ma, J., Chen, B., Wang, L., and Cui, G. (2018). Progress and prospect on failure mechanisms of solid-state lithium batteries. J Power Sources *392*, 94-115. https://doi.org/10.1016/j.jpowsour.2018.04.055.
38. Jung, S.H., Kim, U.-H., Kim, J.-H., Jun, S., Yoon, C.S., Jung, Y.S., and Sun, Y.-K. (2020). Ni-Rich Layered Cathode Materials with Electrochemo-Mechanically Compliant Microstructures for All-Solid-State Li Batteries. Advanced Energy Materials *10*, 1903360. https://doi.org/10.1002/aenm.201903360.
39. Tian, H.-K., and Qi, Y. (2017). Simulation of the Effect of Contact Area Loss in All-Solid-State Li-Ion Batteries. J Electrochem Soc *164*, E3512-E3521. 10.1149/2.0481711jes.
40. Thomas F. Fuller, M.D., John Newman (1994). Simulation and Optimization of the Dual Lithium Ion Insertion Cell. J. Electrochem. Soc. *141*. 10.1149/1.2054684.
41. Bucci, G., Swamy, T., Chiang, Y.-M., and Carter, W.C. (2017). Modeling of internal mechanical failure of all-solid-state batteries during electrochemical cycling, and implications for battery design. J. Mater. Chem. A *5*, 19422-19430. 10.1039/c7ta03199h.
42. Xu, R., Yang, Y., Yin, F., Liu, P., Cloetens, P., Liu, Y., Lin, F., and Zhao, K. (2019). Heterogeneous damage in Li-ion batteries: Experimental analysis and theoretical modeling. J. Mech, Phys. Solids *129*, 160-183. 10.1016/j.jmps.2019.05.003.
43. Koerver, R., Zhang, W., de Biasi, L., Schweidler, S., Kondrakov, A.O., Kolling, S., Brezesinski, T., Hartmann, P., Zeier, W.G., and Janek, J. (2018). Chemo-mechanical expansion of lithium electrode materials – on the route to mechanically optimized all-solid-state batteries. Energy Environ. Sci. *11*, 2142-2158. 10.1039/c8ee00907d.
44. Li, R., Li, W., Singh, A., Ren, D., Hou, Z., and Ouyang, M. (2022). Effect of external pressure and internal stress on battery performance and lifespan. Energy Storage Mater. *52*, 395-429. 10.1016/j.ensm.2022.07.034.
45. Wang, M.J., Choudhury, R., and Sakamoto, J. (2019). Characterizing the Li-Solid-Electrolyte Interface Dynamics as a Function of Stack Pressure and Current Density. Joule *3*, 2165-2178. 10.1016/j.joule.2019.06.017.
46. Doux, J.M., Nguyen, H., Tan, D.H.S., Banerjee, A., Wang, X., Wu, E.A., Jo, C., Yang, H., and Meng, Y.S. (2019). Stack Pressure Considerations for Room-Temperature All-Solid-State Lithium Metal Batteries. Adv. Energy Mater. *10*. 10.1002/aenm.201903253.
47. Sharma, N., Meng, D., Wu, X., de Vasconcelos, L.S., Li, L., and Zhao, K. (2023). Nanoindentation measurements of anisotropic mechanical properties of single crystalline NMC cathodes for Li-ion batteries. Extreme Mech. Lett. *58*. 10.1016/j.eml.2022.101920.
48. Li, Y., Zhang, D., Xu, X., Wang, Z., Liu, Z., Shen, J., Liu, J., and Zhu, M. (2021). Interface engineering for composite cathodes in sulfide-based all-solid-state lithium batteries. Journal of Energy Chemistry *60*, 32-60. 10.1016/j.jechem.2020.12.017.
49. Han, Y., Jung, S.H., Kwak, H., Jun, S., Kwak, H.H., Lee, J.H., Hong, S.-T., and Jung, Y.S. (2021). Single- or Poly-Crystalline Ni-Rich Layered Cathode, Sulfide or Halide Solid Electrolyte: Which Will be the Winners for All-Solid-State Batteries? Adv. Energy Mater. *11*. 10.1002/aenm.202100126.